Effects of Annealing Temperature and Dopant Concentration on the Structural, Optical, and Magnetic Properties of Iron-Doped ZnO Samples

S.A. Ahmed

***Abstract*— This paper reports on the structural, optical, and magnetic properties of as-prepared and annealed $Zn_{1-x}Fe_xO$ ($0.02 \leq x \leq 0.08$) powders synthesized using the solid-state reaction method. X-ray diffraction (XRD) studies showed that Fe was incorporated into the ZnO lattice. Ultraviolet-Visible (UV-vis) spectrophotometry measurements revealed that the bandgap initially increased and then decreased with Fe doping. Photoluminescence (PL) studies confirmed the formation of oxygen vacancies (V_O) in all of the samples. All of the samples exhibited ferromagnetic behavior at room temperature (RT). Ferromagnetic behavior decreased with increased Fe concentrations, due to the increase in the number of Fe atoms occupying the neighboring cation lattice sites, which resulted in an antiferromagnetic configuration. Ferromagnetic behavior also decreased with the increase in the annealing temperature (T_A) due to the reduction of defects and/or V_O. However, our results indicate that the ferromagnetic property is intrinsic to the ZnO system due to defects and/or V_O, and the extrinsic impurity origin was excluded..**

***Index Terms*— Spintronics; Fe-doped ZnO; Optical properties; Magnetic properties; Oxygen vacancy; Ferromagnetism**.

I. Introduction

Dilute magnetic semiconductors (DMSs), which are fabricated by doping the semiconductor with a very small quantity of transition metal (TM) elements into non-magnetic semiconductors, are receiving attention due to their possible application in spin electronics [1]. Wide-gap DMS materials combine electrical conductivity with ferromagnetism and optical transparency, thus paving the way for their potential application in other devices. A wide-band-gap wurtzite-phase semiconductor ZnO (E_g ~3.4eV) doped with TMs has been theoretically predicted to be one of the most favorable DMS materials for room temperature (RT) applications [2]. Ferromagnetism (FM) above RT has previously been predicted theoretically [2,3], and it has been proven experimentally for TM dopants in ZnO. Although RT FM has been observed in ZnO that has been doped with different TMs, the results remain controversial for transition metal-doped ZnO. Karmakar et al. [4] reported weak RT FM in Fe-doped ZnO nanocrystals, and they attributed it to Zn vacancies (V_{Zn}). Recently, Kumar et al. [5] have also reported weak RT FM in $Zn_{0.96}Fe_{0.04}O$ nanocrystals. Mishra and Das [6] investigated RT FM in Fe-doped ZnO nanocrystals, and they suggested that V_{Zn} is responsible for the ferromagnetic order. Johnson et al. [7] and Singh et al. [8] have reported intrinsic RT FM in Fe-doped ZnO nanoparticles, and they attributed it to oxygen vacancies (V_O). Wu et al. [9] suggested that the FM of Fe-doped ZnO film was attributed to the indirect coupling of Fe ion pairs through V_O defects. Recently, Pazhanivelu et al. proposed that, the magnetic behavior of the Li-, Na-, and K-codoped ZnO:Fe nanoparticles depends upon the topology of the grain boundary networks as well as on the solubility of dopant ions in ZnO at the grain and grain boundary regions [10]. On the other hand, Wang et al. [11] have shown RT FM in Fe-doped ZnO nanocrystals, and they suggested that this RT FM resulted from the secondary phase. Whereas, Mandal et al. [12] found that the secondary phase is not responsible for magnetism in $Zn_{1-x}TM_xO$ (TM=Co, Mn, Fe, and Ni) nanocrystalline powder; however, they only observed FM in Fe-doped ZnO at 5 K, while Co-, Mn- and Ni-doped ZnO did not show any ferromagnetic behavior. Therefore, the origin of ferromagnetic ordering in TM-doped ZnO is far from being understood.

Very recently we have performed the detailed experimental studies of the $Zn_{0.98}Fe_{0.02}O$ nanoscale powders [13], which have provided a strong support for "intrinsic" origin of ferromagnetism in the Fe-doped ZnO powders, that is ascribed to the presence of oxygen vacancy defects. In the present work, to clarify the effect of the doping concentration and annealing temperature (T_A), we extended our study to Fe-doped ZnO, varied the doping concentration, and annealed the samples at two temperatures. Therefore, the present investigation provides details on the effects of dopant concentration and T_A on the structure, optical characteristics, and magnetic properties of $Zn_{1-x}Fe_xO$ ($0.02 \leq x \leq 0.08$) nanopowders that are synthesized using a solid-state method. With the help of photoluminescence (PL) results, we have illustrated that V_O^+ (singly charged oxygen vacancies) is the key element for the RT FM in our samples. The presence of the very high oxygen vacancy concentration in the sample gives rise to the ferromagnetic ordering. This study of ZnO:Fe nanoscale powders is expected to contribute to a better understanding of ferromagnetic behavior in Fe-doped ZnO materials.

Manuscript received Jun 30, 2017.

S. A. Ahmed is with the Physics Department, Faculty of Science, Sohag University, Sohag 82524, Egypt (e-mail: saadzf2003@gmail.com).

He is now with the Physics Department, College of Arts and Science, Qassim University, P.O. 3137, Unayzah 51911, Saudi Arabia.

II. Experimental Details

A. Preparation of the Fe-doped ZnO nanopowders

The $Zn_{1-x}Fe_xO$ ($0.02 \leq x \leq 0.08$) nanopowders (ZF2, ZF4, ZF6, and ZF8 for x= 2, 4, 6, and 8 at. %, respectively) were synthesized using the solid-state reaction method. Details of the sample preparation procedures have been described elsewhere [13,14]. To gain more insight into the origin of the ferromagnetic behavior, annealing treatments were carried out in air (12 h) at two different temperatures of 600 and 700ºC for ZF2 (hereafter referred as ZF2-600 and ZF2-700, respectively).

B. Characterization of the materials

The crystalline structure of the samples was characterized by X-ray diffraction (XRD) (PANalytical X'Pert PRO). The optical absorption was measured at RT using a CARY 5000 ultraviolet-visible (UV–vis) spectrophotometry with a wavelength ranging from 200-800 nm. The RT-PL spectra were measured in the range of 400-800 nm using a luminescence spectrometer (CARY Eclipse) at 381 nm. The magnetic properties (M(H)) of the samples were examined using a Lakeshore vibrating sample magnetometer (VSM) (model no. 7410).

III. Results and Discussion

A. X-ray diffraction analysis

The crystallographic structure (formation of phase(s) and structural transformation) of ZnO both with different Fe content (ZF2, ZF4, ZF6, and ZF8) and annealing temperatures (ZF2-600 and ZF2-700) was examined using X-ray diffractograms, as presented in Fig. 1. For comparison, the XRD pattern for undoped ZnO sample (prepared under the same conditions as the doped samples) is also shown in Fig. 1. The XRD data demonstrate that the ZF2, ZF4, ZF6, ZF8, ZF2-600, and ZF2-700 samples have the wurtzite-phase of ZnO (JCPDS file no. 36–1451). The XRD intense planes (*h k l*) for all of the samples are: (100), (002), (101), (102), (110), (103), (200), (112), (201), (004), and (202), respectively. Prominent lines at 31.80º, 34.45º, 36.28º, 47.56º, 56.59º, 62.86º, 66.37º, 67.95º, 69.09º, 72.57º, and 76.97º, respectively, are indicated on the diffraction peaks (Fig. 1). In addition to the dominant hexagonal-$Zn_{1-x}Fe_xO$, very small peaks representing other secondary phases were observed in the XRD spectra, which are indicated in Fig. 1.

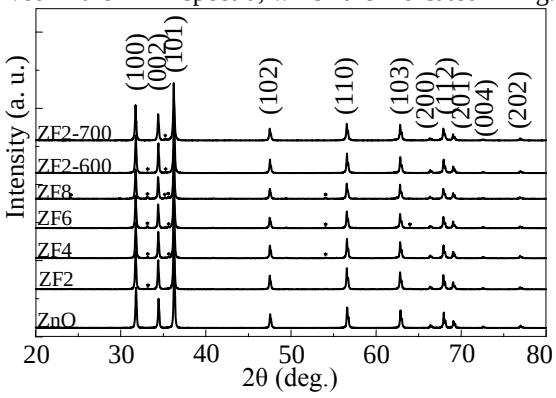

Fig. 1. RT *θ-2θ* XRD patterns of ZF2-ZF8, ZF2-600, and ZF2-700 Fe-doped ZnO samples. The marks **"⋆"** and **"♦"** respectively represent α-Fe_2O_3 and $ZnFe_2O_4$ impurity phase in the sample..

As seen in Fig. 1, the α-Fe_2O_3 impurity phase peaks evolve as extra planes at 24.14º, 33.14º, 35.63º, 54.02°, and 64.02º; and with h k l as: 012, 104, 110, 116, and 300, respectively (JCPDS file no. 89–8104), as denoted by **"⋆"** in Fig. 1, along with hexagonal-ZnO. This is consistent with earlier observations that the solubility of Fe in the ZnO crystal lattice is below 2 at. % [15] or less than 1 at. % [16]. The XRD results for the ZF8 sample also show a minuscule peak that evolves as extra plane at 35.19º, as denoted by **"♦"** in Fig. 1; corresponds to the (311) plane of the secondary phase of $ZnFe_2O_4$ (JCPDS file no. 22–1012). However, this implies the formation of the secondary phase of α-Fe_2O_3 impurity phase peaks, while the $ZnFe_2O_4$ secondary phase was only observed in the ZF8 sample, in addition to the dominant hexagonal-ZnO phase of $Zn_{1-x}Fe_xO$, which occurs for all of the Fe concentrations. Note that the intensity of the α-Fe_2O_3 phase increases with the increase of Fe-doping. As compared to the ZF2 sample, in addition to the (104) orientation peak of the α-Fe_2O_3 phase, another peak for the $ZnFe_2O_4$ phase with (311) orientation was observed in the ZF2-600 sample, while only the (311) orientation peak of the $ZnFe_2O_4$ phase were detected for the ZF2-700 sample (Fig. 1). However, careful analysis of the XRD peak positions shows a slight shifting of the diffraction peaks toward a lower 2θ value with Fe-doping (Fig. 1). The 2θ degrees of the ZnO (002) diffraction peak are 34.452º, 34.404º, 34.415º, 34.401º, and 34.397º for ZnO, ZF2, ZF4, ZF6, and ZF8, respectively. Nevertheless, a shift towards a lower angle was observed for all of the strong peaks with the increase in Fe concentration in the ZnO structure. A similar observation has been reported by other researchers, and this has been interpreted as being due to the incorporation of dopant ions into the lattice of the host material [5,6]. As for the ZF2-600 and ZF2-700 samples, the 2θ degrees of the ZnO (002) diffraction peak are 34.424º and 34.397º, respectively. It is obvious that the diffraction peaks shifted to higher/lower angles when T_A increased from 600 to 700ºC, respectively, with respect to the sample annealed at 500ºC. Still, the diffraction peak at 34.424º of the ZF2-600 sample clearly shows a shift to a lower angle in comparison to the diffraction peak at 34.452º of the ZnO sample. However, for the ZF2-ZF8 samples, the peaks were also found to broaden with the increase of Fe in ZnO, which has been explained as being due to the reduction of crystallite size with the incorporation of Fe-atoms. It appears that the incorporation of Fe into the ZnO structure reduces the grain growth that causes a reduction in the average crystallite size, which was also reported in others studies [5,6,17]. In this present study, the lattice parameters (**a** and **c**) and the average crystallite sizes (**D**) were calculated using Equations (1) and (2), respectively:

$$sin^2\theta = \frac{\lambda^2}{4}\left[\frac{4}{3}\left(\frac{h^2+hk+l^2}{a^2}\right)+\frac{l^2}{c^2}\right], \quad (1)$$

where θ is the diffraction angle, λ is the incident wavelength (λ=1.5406 Å), and h, k, and l are Miller's indices; and

$$D = \frac{0.9\lambda}{\beta cos\theta}, \quad (2)$$

where d is the mean grain size, K is the shape factor (usually taken as 0.89), λ is the X-ray wavelength of Cu-$K\alpha_1$ radiation in nm (λ=0.15406 nm), β is the instrument-corrected full-width-at-half maximum (FWHM) of the XRD peak, and θ is the Lorentz-shaped Bragg's angle.

The lattice parameters, **a** and **c**, as well as the unit cell volume (**V**) obtained from the XRD patterns of the ZF2-ZF8 samples, are summarized in Table 1; these increased due to

Fe-doping in ZnO, suggesting the incorporation of Fe ions (in the high spin state, F^{2+} [18]) into the lattice of the hexagonal wurtzite structure phase of ZnO. A similar feature was observed for the unit cell volume, indicating that the lattice increases and the unit cell become higher with increasing Fe concentration from ZF2 to ZF8. The increase in the lattice parameters can be understood as the increase of the mean ionic radius at the Zn-site (Fe^{2+} (0.63 Å)/Zn^{2+} (0.60 Å)), both in the tetrahedral coordinate, with the increase in Fe^{2+} content from ZF2 to ZF8. It is worth mentioning that, in a stoichiometric wurtzite structure, the **c**/**a** ratio is 1.633. Here, all of the samples showed a significantly smaller **c**/**a** ratio (1.601±0.001), and this might indicate the presence of V_O and extended defects [19]. As for the ZF2 samples annealed at different T_A, the lattice parameters and the cell volume of the ZF2-600 and ZF-700 samples are higher than those of the ZF2-500 sample, as shown in Table 1.

TABLE I
VARIATION OF LATTICE PARAMETERS (A AND C) AND CELL VOLUME (V) OF ZNO, ZF2-ZF8, ZF2-600, AND ZF2-700 FE-DOPED ZNO SAMPLES.

Samples	Lattice		Grain size
	parameter (Å)	volume (Å^3)	(nm)
ZnO	a=3.2495; c=5.2065	47.60	27.47
ZF2	a=3.2544; c=5.2090	47.76	26.05
ZF4	a=3.2545; c=5.2098	47.77	26.01
ZF6	a=3.2546; c=5.2125	47.80	25.83
ZF8	a=3.2548; c=5.2128	47.81	25.09
ZF2-600	a=3.2545; c=5.2106	47.78	26.26
ZF2-700	a=3.2547; c=5.2146	47.82	26.53

The average volume-weighted crystallite size **D** of ZF2-ZF8 was evaluated using the peak broadening FWHM technique (every ZnO peak in the spectra was fitted with a Gaussian function) and Scherrer's Eq. (2). The evaluated crystallite size of ZF2-ZF8 as a function of the Fe concentration is shown in Table 1. As seen from Table 1, the samples are nanocrystalline with a **D** of 27.47–25.09 nm; moreover, as the Fe concentration increases, **D** is gradually reduced from its value in the undoped ZnO sample, and this appears to be strongly connected to the change in the Fe content. The **D** calculations for the ZF2 samples annealed at a T_A of 500, 600, and 700ºC (ZF2-500, ZF2-600, and ZF2-700) indicate a small improvement from 26.05 nm to 26.53 nm when T_A increased from 500 to 700ºC; this implies that only limited sintering occurred. This could be due to the formation of the $ZnFe_2O_4$ secondary phase in the samples that were annealed at 600 and 700ºC, in addition to a significant suppression in the V_O concentration during the annealing process, as shown in [14,20]. In the nanocrystalline phase, since the surface-to-volume ratio is very high, the surface defects play an important role. These defects have some impact on the grain size development (prevent grain growth) with T_A. The presence of nanoscale grain size with more defects on the surface and grain boundary restrain grain growth [21]. However, these findings are compatible with the PL results (discussed below in Section III.B.2). Nevertheless, the shifting of the XRD patterns, the increased lattice parameters, and the reduction of **D** with the increase of Fe concentration from ZF2 to ZF8 suggest that the Fe^{+2} ions were successfully incorporated into the ZnO lattice at the Zn^{+2} sites (the Fe ion replacing the Zn ion in the crystallographic structure).

B. Optical characterization and defect analysis:

1. Optical absorption

The RT UV–Vis absorption spectra for all the samples in the 200–800 nm range are shown in Fig. 2(a). A blue shift in the absorption edge was observed in the ZF2, ZF6, ZF2-600, and ZF2-700 samples compared to that of ZnO, which confirms that Fe was incorporated into the ZnO structure [6].

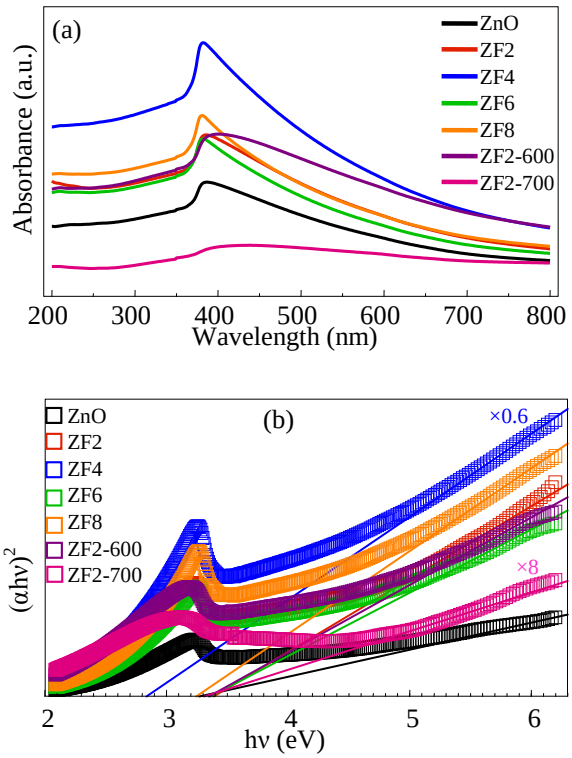

Fig. 2. a RT UV-Vis absorption spectra and b $(\alpha h\nu)^2$ vs. hν of ZF2-ZF8, ZF2-600, and ZF2-700 Fe-doped ZnO samples.

This increase in the bandgap was elucidated through the Burstein-Moss band filling effect [16]. In addition, the ZF4 and ZF8 samples show a red shift for the undoped material [17]. This red shift behavior, or the contraction in the bandgap for the ZF4 and ZF8 samples, can be interpreted as being due to the *s–d* and *p–d* exchange interactions between the band electrons of ZnO and the localized *d* electrons of the Fe ions that arise as these ions replace the Zn^{2+} ions. The optical energy bandgap, E_g, of the samples was estimated using the Tauc relation:

$$(\alpha h\nu)\sim(h\nu - E_g)^{1/2}, \quad (3)$$

where $h\nu$ is the photon energy and α is the optical absorption coefficient. We have estimated E_g from the linear fit in the experimental curves using Eq. (3), setting the boundary condition [$(\alpha h\nu)^2$=0, $h\nu$=E_g] for each curve with different Fe^{2+} doping concentrations (x), as shown in Fig. 2(b). As seen in that figure, E_g of the ZF4 sample is 2.84 eV, which is lower than that of the undoped ZnO (3.27 eV) [13], whereas the ZF2 sample has an E_g of 3.39 eV. The bandgap values for the ZF6, ZF8, ZF2-600, and ZF2-700 samples are 3.36, 3.25, 3.35, and 3.31 eV, respectively. The change of E_g with Fe-doping ZnO and T_A indicates that the Fe cation has successfully been incorporated into the ZnO crystal lattice [17], verifying that the obtained FM signals (discussed in Section III.C, which addresses magnetic properties) arise from the Fe substitution, not from impurities. A similar

red-blue shift in the energy bandgap of the Fe-doped ZnO sol-gel nanoparticles was reported by Kumar et al. [5]. Sahai et al. [16] observed a blue shift in the bandgap in Fe-doped ZnO nanostructures that were synthesized using a chemical precipitation route. A blue shift in the energy bandgap of the Fe-doped ZnO nanoparticles was also reported by Singh et al. [8]. Saleh et al. [22] also found a reduction of bandgap in Fe-doped nanocrystalline ZnO particles that were synthesized using the co-precipitation method.

2. Photoluminescence analysis

In this present study, the RT PL spectra of all the samples were acquired using an excitation line of 381 nm, as presented in Fig. 3. The PL spectra of all the samples display three emission bands, a predominant violet emission, a quenched blue emission, and a strong green emission. It is important to note that all of the PL emissions are from the ZnO nanopowders. Moreover, Fe doping does not change the peak positions in the ZnO PL spectra. In comparison to the undoped ZnO sample, the intensity of the PL emissions increase after Fe is introduced into the doped sample. This indicates that Fe doping increases the radiative recombination processes. A similar result for Fe-doped ZnO nanoparticles was reported in a previous study [5]. In the present study, the intensity of the PL emissions slightly increased after the ZF2 sample annealed at 600ºC (ZF2-600) with respect to the ZF2-500 sample. The PL intensity increased in the ZF2-600 sample as non-radiative defects are less in this sample. Annealing ZnO:0.02Fe at 600ºC at RT removed many of the non-radiative V_O on the surface and on the grain boundary. Consequently, more electron–hole pairs recombine through radiative recombination than through non-radiative recombination. Additionally, a decrease in the concentration of the charged defect centers reduces the possibility of mobile electron scattering, resulting in easy recombination of the carriers, thus, to some extent, leading to the PL enhancement. In contrast, annealing the Zn:0.02Fe sample at 700ºC (ZF2-700) induced a decrease in the emission peaks. This behavior might occur because the V_O reduction, which is responsible for the radiative transition, during the annealing process at 700ºC, has an impact on the PL intensity, which decreased upon annealing at 700ºC. At 700ºC, both the radiative V_O and the non-radiative V_O decreased. Note that excitonic emissions with a small exciton Bohr radius of 1.8 nm are more sensitive to imperfections of the microstructure of a crystal, while XRD is mainly affected by the crystal size.

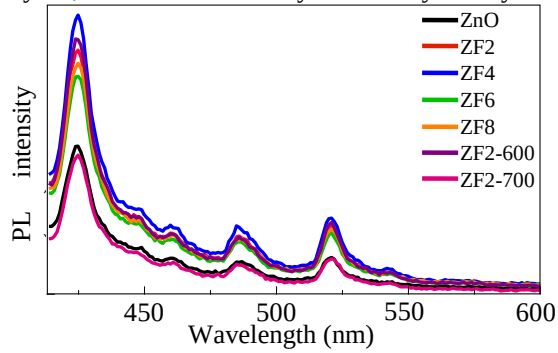

Fig. 3. RT PL spectra of ZF2-ZF8, ZF2-600, and ZF2-700 Fe-doped ZnO samples.

The green emission around 486 nm (2.55 eV) and 521 nm (2.38 eV) is attributed to the recombination of electrons trapped in singly-ionized V_O (V_O^+) with photogenerated holes [23-25]. The singly-charged center (V_O^+) in the absence of a depletion region becomes the neutral center (V_O^x) via the capture of an electron from the conduction band, which then recombines with a hole in the valence band giving rise to emissions at 486 nm (2.55 eV) and 521 nm (2.38 eV) [26]. The blue emission around 448 nm (2.77 eV) and 461 nm (2.69 eV) can be assigned to the intrinsic V_O^x defects [27,28], which act as a trap for the photogenerated holes. The V_O of ZnO has been predicted to be at ~ E_V+2.7 eV [29] or ~ E_V+2.78 eV [27], which is consistent with the photon energy of the blue emissions observed in this present study. In bulk ZnO, the V_O^x centers are not underactive ionized, which is a response to the absence of blue emission in bulk ZnO [27]. The violet luminescence around 424 nm (2.92 eV) is probably due to the V_O^x [5,30,31] radiative defects related to the interface traps that exist at the grain boundaries [23,24] of ZnO and that are emitted from the radiative transitions between these levels and the valence band. In our study, the XRD results (Fig. 1) indicate that the samples have a nanocrystalline structure with a high surface-to-volume ratio, which may also suggest that the number of interface traps can be increased due to the expansion of the regions between the ZnO grains [32]. In other words, the samples may have more grain boundary defects that emit the violet luminescence with a higher intensity because they have smaller grains and a larger grain boundary area. Furthermore, Cordaro et al. have reported that the interface traps (the V_O), located within the depletion regions at the ZnO-ZnO grain boundaries, have been found to be about 0.33 eV below the conduction band edge [33].

The violet emission was also assigned to interstitial zinc (Zn_i) [6] while the blue emission was attributed to Zn_i [16] or V_{Zn} [5]. Zn_i has high formation energy even under Zn-rich conditions. According to [34], the V_O should predominate in Zn-rich crystals since their formation energy is lower than the formation energy of Zn_i. This implies that, under equilibrium conditions, Zn_i will be present in low concentrations and it cannot to be responsible for the predominant violet emission in our samples, as shown in Fig. 3. V_{Zn} point defects may be thermodynamically established in the ZnO crystal lattice, but at a higher oxygen partial pressure [35]. Meanwhile, a Zn_i point defect has been demonstrated experimentally to be a very unstable defect [36]. Moreover, Sanyal et al. [37] and Dutta et al. [38] showed that a significant number of V_O were produced and Zn_i atoms acquired sufficient energy and returned to the crystal lattice site (i.e., Zn_i recombined with V_{Zn}) by annealing the polycrystalline ZnO in the air at about 500ºC. Recently, Liu [39] also demonstrated that when annealing ZnO:Co films in the air at 600ºC, the Zn_i atoms are returned to the crystal lattice site. Mishra et al. [40] reported that the Zn_i defects are highly mobile at and above 400ºC, and they are likely to recombine with the V_{Zn} that is dominant in ZnO nanocrystal grain boundaries. Note that all of the samples in our case were annealed in ambient air, resulting in an oxygen-deficient ZnO crystal [13,14,37,38]; consequently, the visible emission is most likely connected to the oxygen vacancy defects, and it can be clear that the samples have plenty of V_O.

C. Magnetic measurements (VSM)

Next, we discuss the magnetic properties of $Zn_{1-x}Fe_xO$ nanopowders, as evaluated using VSM. The magnetization loops of the ZF2-ZF8 samples were measured at 300 K using a VSM magnetometer, and the M(H) curves, with their corresponding expanded view of the hysteresis loops near the origin, are shown in Fig. 4 and its inset (i). The diamagnetic contribution from the sample holder has already been subtracted to estimate the actual FM contribution of each sample. Hysteresis loops can be observed clearly in the M(H) curves of the ZF2-ZF8 samples, thus indication FM hysteresis. The hysteresis loops indicate that the ZF2-ZF8 samples have RT FM. The magnetization data recorded for the undoped ZnO showed very weak but distinct evidence of magnetic ordering, with an apparent FM saturation moment of 0.08 x 10^{-3} μ_B (f.u.)$^{-1}$ (5.52 x 10^{-3} emu g^{-1}) and coercivity of 258 Oe at 300 K [13]. It was assumed that V_O^+, located on the surface with an unpaired electron in the nanopowder samples must be responsible for the induced magnetism in the undoped ZnO. Very strong RT FM was observed when the undoped ZnO was doped with 2, 4, 6, and 8 at. % Fe nanopowder samples, as shown in Fig. 4, after the linear response term (paramagnetic (PM) component) was removed from the raw data. As evident from Fig. 4 and its inset (i), the

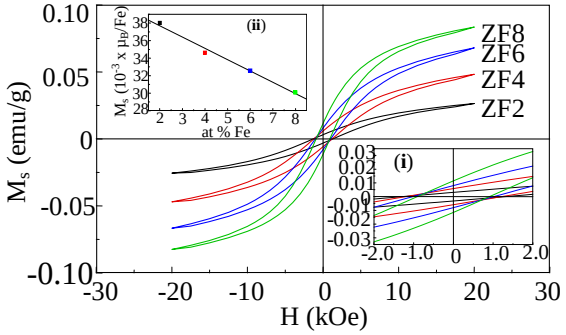

Fig. 4. RT M-H curves of ZF2-ZF8 Fe-doped ZnO samples. The insets (i) and (ii) respectively show the RT hysteresis in the low-field region and the variation of M_s (μ_B/Fe) with at. % Fe.

ZF2 sample has a well-defined hysteresis loop at 300 K with a coercive field (H_c) of 1295 Oe and a remnant magnetization (M_r) of 0.003 emu g^{-1}. However, both the M_r and the saturation magnetization (M_s) increased and the H_c decreased with the increase in the Fe-doping concentration from 2 at. % (ZF2) to 8 at. % (ZF8). The 300 K M_s of the ZF2-ZF8 samples are 0.027, 0.048, 0.068, and 0.084 emu g^{-1} for the ZF2, ZF4, ZF6, and ZF8 samples, respectively. The M_r of the ZF2-ZF8 samples follows a similar trend: M_r=0.003, 0.006, 0.008, and 0.012 emu g^{-1}, respectively, at 300 K. However, the low M_s value must be ascribed to the low fraction of Fe ions involved in FM ordering, and the fact that most of the Fe ions remained in a PM state, in addition to the antiferromagnetic (AFM) state related to the impurity phase inside the sample [4,6]. It is important to note that the M_s values for the ZF2-ZF8 samples are higher than the M_s value for the ZnO:0.02Fe powders (0.02 emu g^{-1} [41] and 0.015 emu g^{-1} [42]) that were synthesized using the solid-state reaction method, ZnO:0.10Fe nanoparticles (0.018 emu g^{-1}) that were prepared using the chemical hydrolysis method [7], and ZnO:0.04Fe nanoparticles (0.005 emu g^{-1}) that were synthesized using the sol–gel method [5]. The M_r values for the ZF2-ZF8 samples are similar to or higher than the M_r value for the ZnO:0.05Fe nanocrystalline particles (0.006) that were synthesized using the co-precipitation method [22], ZnO:0.07Fe nanoparticles (5.15 × 10^{-3} emu g^{-1}) that were synthesized via a chemical route [6], and ZnO:0.02Fe powders (1.816 × 10^{-3} emu g^{-1}) that were synthesized using the solid-state reaction method [42]. The 300 K H_c of the ZF2-ZF8 samples are 1295, 1210, 1020, and 910 Oe for the ZF2, ZF4, ZF6, and ZF8 samples, respectively (inset (i) of Fig. 4). The high coercivity fields obtained seem to result in a potential candidate for spintronic applications. The H_c values of the ZF2-ZF8 samples are higher than the H_c value, 700 Oe, of the ZnO:0.04Fe nanoparticles [5], but they are smaller than the H_c value, 1984 Oe, of the ZnO:0.07Fe nanoparticles [6]. The presence of clear H_c rules out the possibility of superparamagnetism and supports the FM origin [7]. Also, we discounted the segregation of the metallic Fe phase as the origin of FM because the solid-state reaction method based synthesis intrinsically eliminates the possible formation of metal clusters due to its aerobic nature [13]. In addition, strong reducing conditions are needed in order for the metallic Fe phase to be segregated [18]. On the other hand, the maghemite (γ-Fe_2O_3) phase converted to the hematite (α-Fe_2O_3) phase when the sample was annealed at temperatures above 350°C [43,44]. Additionally, the hematite phase is thermally the most stable phase, and it undergoes a thermal reduction to the magnetite (Fe_3O_4) phase only above 1200°C [44]. By recalling the XRD data that was previously discussed, which clearly rule out the possible presence of metallic Fe, only the α-Fe_2O_3 and $ZnFe_2O_4$ secondary phases were observed. Both the α-Fe_2O_3 and $ZnFe_2O_4$ secondary phases are normally nonmagnetic at RT [4,6]. Furthermore, the random presence of α-Fe_2O_3 and $ZnFe_2O_4$ impurities is unlikely to produce a similar magnetization with high H_c values in the range of 1295-910 Oe. For all the above reasons, we believe that FM in our samples is an intrinsic property; it is not due to the presence of iron phase impurities [7,13]. Figure 4 inset (ii) shows the 300 K magnetic moment per Fe ion dependence of the Fe concentration (the magnetic moment per atom was evaluated by considering the nominal concentration of the magnetic ions). However, the magnetic moment was linearly decreased from 0.038 μ_B Fe^{-1} ion for the 2 at. % Fe-doped ZnO (ZF2) to 0.030 μ_B Fe^{-1} ion for the 8 at. % Fe-doped ZnO (ZF8), as shown in Fig. 4 inset (ii). These magnetic moment values are far below the full magnetic moment due to the Fe^{2+} ion. This clearly indicates that only a small fraction of the substituted Fe contributes to the long-range ferromagnetic order. The decrease in the magnetic moment with the increase in Fe concentration can be attributed to the formation of AFM Fe clusters due to the decreased Fe–Fe distance [4]. The enhanced AFM interaction between neighboring Fe-Fe ions suppresses the FM with the increase in the Fe-doping concentration. The decrease in the FM moment that occurs with the increase in the Fe concentration also supports the finding that the observed hysteresis cannot be attributed to FM impurity phases. If that has occurred, an increase in the Fe content would have increased the volume fraction of the secondary phase and the corresponding magnetization features, which is not the case. Instead, the opposite behavior was observed (refer to inset (ii) of Fig. 4). Therefore, the observed FM in the ZF2-ZF8 samples is an intrinsic property; is not due to the Fe clusters or impurity phases, and it might be

related to variations in the sample defect structure and/or V_O [4,9,45,46].

The magnetization of the samples can be changed by post-annealing at different annealing temperatures. Figure 5 shows the M(H) curves at 300 K for the ZF2 samples annealed at 600 and 700ºC (ZF2-600 and ZF2-700) with their corresponding low-field regions (Fig. 5 inset (i)), indicating FM hysteresis. For a direct comparison, the M(H) curve of the ZF2-500 sample is also displayed in Fig. 5. Annealing in air eliminates the V_O of the samples. The magnetization decreased as the T_A increased (Fig. 5). For annealing above 500ºC, the M_s per Fe ion linearly decreased with increasing T_A, as shown in Fig. 5 inset (ii). It is clear that the ZF2-600 and ZF2-700 samples were FM; their, M_s values were 23.45 x 10^{-3} emu g^{-1} (0.034 μ_B Fe^{-1}) and 21.10 x 10^{-3} emu g^{-1} (0.030 μ_B Fe^{-1}), respectively; their M_r values were 2.05 x 10^{-3} and 0.90 x 10^{-3} emu g^{-1}, respectively; and their H_c values were, respectively 805 and 370 Oe (Fig. 5 inset (i)). It seems that the FM properties of the $Zn_{1-x}Fe_xO$ samples as a function of T_A confirm that defects and/or V_O can strongly affect the FM in the ZnO:Fe system.

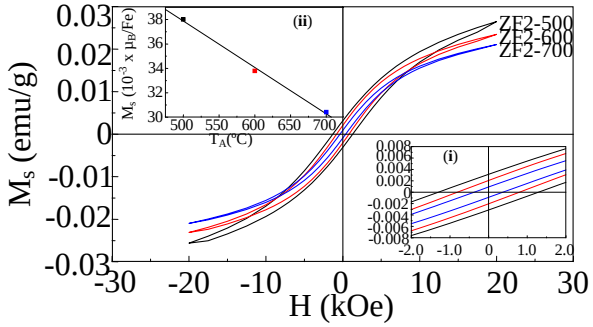

Fig. 5. RT M-H curves of ZF2-500, ZF2-600, and ZF2-700 Fe-doped ZnO samples. The insets (i) and (ii) respectively show the RT hysteresis in the low-field region and the variation of M_s (μ_B/Fe) with T_A.

Based on the above analysis, it appears that the magnetism of the $Zn_{1-x}Fe_xO$ samples strongly depends on the doping content and T_A. The M_s per Fe ion decreased as the Fe concentration increased due to an increase in the fraction of the AFM-coupled atoms. The competition between FM and AFM led to the decrease in M_s per Fe ion with increasing Fe concentration. Moreover, decreasing M_s with increasing T_A demonstrated that T_A played an important role in the magnetic properties of the Fe-doped ZnO samples. Therefore, we can argue that both the number of V_O and the distance between the Fe ions play important roles in the origin of magnetism. However, it is clear from a wide variety of experimental results that point defects, that is, V_O (V_O^+) (unpaired electrons), are responsible for the FM response present in the undoped samples and the TM-doped ZnO samples [4,9,10,45]. The formation of V_O (V_O^+) is clearly evident from the PL spectra of all the samples. From the above observations and the PL results, we suggest that singly-charged V_O (V_O^+) located on the surface with an unpaired electron and localized "**d**" spins on the Fe ions are responsible for the RT FM of Fe-doped ZnO nanopowders. This correlation favors the formation of bound magnetic polarons as the origin of RT FM [3,13,25]. According to this theory of defect-mediated RT FM, bound electrons in V_O (V_O^+) can couple with Fe ions and cause ferromagnetic ordering.

IV. 4 Conclusions

In this study, Fe-doped ZnO nanopowders were successfully prepared using the solid-state reaction method. XRD studies indicated that Fe was incorporated into the ZnO lattice. UV–Vis measurements revealed that the bandgap initially increased and then decreased with Fe doping. PL studies confirmed the formation of V_O in all of the samples. RT FM was observed with a VSM magnetometer in all of the samples. Ferromagnetic behavior was reduced with the increase in Fe concentration, due to an increase in the number of Fe atoms occupying neighboring cation lattice sites, which resulted in an AFM configuration. Moreover, ferromagnetic behavior decreased with increasing T_A due to the reduction of defects and/or V_O, which reflects the key role played by defects in the stabilization of ferromagnetism in Fe-doped ZnO. However, our results indicate that the FM property is intrinsic to the ZnO system, and the extrinsic impurity origin was excluded. We believe that the FM is intrinsic, and it is probably due to interactions between substitutional Fe_{Zn} and intrinsic point defects, most likely V_O (V_O^+), in the crystal.

References

[1] H. Ohno, "Making nonmagnetic semiconductors ferromagnetic," *Science* 281 (1998) 951–956.

[2] T. Dietl, H. Ohno, F. Matsukura, J. Cibert, and D. Ferrand, "Zener model description of ferromagnetism in zinc-blende magnetic semiconductors," *Science* 287 (2000) 1019–1022.

[3] J.M.D. Coey, M. Venkatesan, and C.B. Fitzgerald, "Donor impurity band exchange in dilute ferromagnetic oxides," *Nat. Mater*. 4 (2005) 173–179.

[4] D. Karmakar, S.K. Mandal, R.M. Kadam, P.L. Paulose, A.K. Rajarajan, T.K. Nath, A.K. Das, I. Dasgupta, and G.P. Das, "Ferromagnetism in Fe-doped ZnO nanocrystals: Experimental and theoretical investigations," *Phys. Rev*. B 75 (2007) 144404.

[5] S. Kumar, S. Mukherjee, R. Kr. Singh, S. Chatterjee, and A.K. Ghosh, "Structural and optical properties of sol-gel derived nanocrystalline Fe-doped ZnO," *J. Appl. Phys*. 110 (2011) 103508.

[6] A.K. Mishra, and D. Das, "Investigation on Fe-doped ZnO nanostructures prepared by a chemical route," *Mater. Sci. Eng*. B 171 (2010) 5–10.

[7] L.M. Johnson, A.P. Thurber, J. Anghel, M. Sabetian, M.H. Engelhard, D.A. Tenne, C.B. Hanna, and A. Punnoose, "Transition metal dopants essential for producing ferromagnetism in metal oxide nanoparticles," *Phys. Rev*. B 82 (2010) 054419.

[8] R.P.P. Singh, I.S. Hudiara, S. Panday, and S.B. Rana, "The effect of Co doping on the structural, optical, and magnetic properties of Fe-doped ZnO nanoparticles," *J. Supercond. Nov. Magn*. 29 (2016) 819-827.

[9] P. Wu, G. Saraf, Y. Lu, D. H. Hill, R. Gateau, L. Wielunski, R.A. Bartynsk, D.A. Arena, J. Dvorak, A. Moodenbaugh, T. Siegrist, J.A. Raley, and Y.K. Yeo, "Ferromagnetism in Fe-implanted a-plane ZnO films," *Appl. Phys. Lett*. 89 (2006) 012508.

[10] V. Pazhanivelu, A.P.B. Selvadurai, R. Kannan, and R. Murugaraj, "Room temperature ferromagnetism in Ist group elements codoped ZnO:Fe nanoparticles by co-precipitation method," *Physica* B 487 (2016) 102–108.

[11] D. Wang, Z.Q. Chen, D.D. Wang, J. Gong, C.Y. Cao, Z. Tang, and L.R. Huang, "Effect of thermal annealing on the structure and magnetism of Fe-doped ZnO nanocrystals synthesized by solid state reaction," *J. Magn. Magn. Mater*. 322 (2010) 3642–3647.

[12] S.K. Mandal, A.K. Das, T.K. Nath, and D. Karmakar, "Temperature dependence of solubility limits of transition metals (Co, Mn, Fe, and Ni) in ZnO nanoparticles," *Appl. Phys. Lett*. 89 (2006) 144105.

[13] S.A. Ahmed, "Effects of Cu and Mn dopings on the structural, optical, and magnetic properties of $Zn_{0.98}Fe_{0.02}O$ nanopowders," *J. Mater. Sci*. 52 (2017) 4977-4987.

[14] S.A. Ahmed, "Effects of annealing temperature and dopant concentration on the structure, optical, and magnetic properties of

Cu-doped ZnO nanopowders," J. *Mater. Sci.: Mater. Electron*. 28 (2017) 3733-3739.

[15] M. Chakrabarti, S. Dechoudhury, D. Sanyal, T.K. Roy, D. Bhowmick, and A. Chakrabarti, "Observation of room temperature ferromagnetism in Mn–Fe doped ZnO," *J. Phys. D Appl. Phys*. 41 (2008) 135006.

[16] A. Sahai, Y. Kumar, V. Agarwal, S.F. Olive-Méndez, and N. Goswami, "Doping concentration driven morphological evolution of Fe doped ZnO nanostructures," *J. Appl. Phys*. 116 (2014) 164315.

[17] P. Sikam, P. Moontragoon, J. Jumpatam, S. Pinitsoontorn, P. Thongbai, T. Kamwanna, "Structural, optical, electronic and magnetic properties of Fe-doped ZnO nanoparticles synthesized by combustion method and first-principle calculation," *J. Supercond. Nov. Magn*. 29 (2016) 3155-3166.

[18] J. Blasco, F. Bartolomé, L.M. García, and J. García, "Extrinsic origin of ferromagnetism in doped ZnO, *J. Mater. Chem*. 16 (2006) 2282–2288.

[19] J.J. Beltrán, J.A. Osorio, C.A. Barrero, C.B. Hanna, and A. Punnoose, "Magnetic properties of Fe doped, Co doped, and Fe + Co co-doped ZnO," *J. Appl. Phys*. 113 (2013) 17C308.

[20] H. Zhang, Z. Wen, X.O. Qi, L.A. Si, L.U. Xu, W. Zhong, D. Wu, K. Shen, M.X. Xu, T. Qiu, and Q.Y. Xu, "H mediated room temperature ferromagnetism in $Zn_{0.98}Cu_{0.02}O$," *J. Alloys Compd*. 536 (2012) 184–188.

[21] B. Choudhury, and A. Choudhury, "Room temperature ferromagnetism in defective TiO2 nanoparticles: Role of surface and grain boundary oxygen vacancies," *J. Appl. Phys*. 114 (2013) 203906.

[22] R. Saleh, S.P. Prakoso, and A. Fishli, "The influence of Fe doping on the structural, magnetic, and optical properties of nanocrystalline ZnO particles," *J. Magn. Magn. Mater*. 324 (2012) 665–670.

[23] K. Prabakar, C. Kim, and C. Lee, "UV, violet, and blue-green luminescence from RF sputter deposited ZnO:Al thin films," *Cryst. Res. Technol*. 40 (2005) 1150–1154.

[24] A.K. Srivastava, M. Deepa, N. Bahadur, and M.S. Goyat, "Influence of Fe doping on nanostructures and photoluminescence of sol–gel derived ZnO," *Mater. Chem. Phys*. 114 (2009) 194-198.

[25] V. Pazhanivelu, A.P.B. Selvadurai, and R. Murugaraj, "Effect of Ni Doping on Structural, Morphological, Optical and Magnetic Properties of $Zn_{1-x}Ni_xO$ Dilute Magnetic Semiconductors," *J. Supercond. Nov. Magn*. 27 (2014) 1737-1742.

[26] M. Ghosh, and A.K. Raychaudhuri, "Shape transition in ZnO nanostructures and its effect on blue-green photoluminescence," *Nanotechnology* 19 (2008) 445704.

[27] Z.-M. Liao, H.-Z. Zhang, Y.-B. Zhou, J. Xu, J.-M. Zhang, and D.-P. Yu, "Surface effects on photoluminescence of single ZnO nanowires," *Phys. Lett*. A 372 (2008) 4505–4509.

[28] R. Wu, Y. Yang, S. Cong, Z. Wu, C. Xie, H. Usui, K. Kawaguchi, and N. Koshizaki, "Fractal dimension and photoluminescence of ZnO tetrapod nanowhiskers," *Chem. Phys. Lett*. 406 (2005) 457–461.

[29] C.G. Van de Walle, "Defect analysis and engineering in ZnO," *Physica* B 308–310 (2001) 899–903.

[30] B.J. Jin, S. Im, and S.Y. Lee, "Violet and UV luminescence emitted from ZnO thin films grown on sapphire by pulsed laser deposition," *Thin Solid Films* 366 (2000) 107–110.

[31] S. Fabbiyola, L.J. Kennedy, T. Ratnaji, J.J. Vijaya, U. Aruldoss, and M. Bououdina, "Effect of Fe-doping on the structural, optical and magnetic properties of ZnO nanostructures synthesized by co-precipitation method," *Ceram. Int*. 42 (2016) 1588–1596.

[32] X.J. Liu, X.Y. Zhu, J.T. Luo, F. Zeng, and F. Pan, "Grain boundary defects-mediated room temperature ferromagnetism in Co-doped ZnO film," *J Alloys Compd*. 482 (2009) 224–228.

[33] J.F. Cordaro, Y. Shim, and J.E. May, "Bulk electron traps in zinc oxide varistors," J. Appl. Phys. 60 (1986) 4186–4190.

[34] A.F. Kohan, G. Ceder, D. Morgan, and C.G. Van de Walle, "First-principles study of native point defects in ZnO," *Phys. Rev*. B 61 (2000) 15019–15027.

[35] F. Tuomisto, V. Ranki, K. Saarinen, and D.C. Look, "Evidence of the Zn vacancy acting as the dominant acceptor in n-type ZnO," *Phys Rev Lett* 91 (2003) 205502.

[36] L.S. Vlasenko, and G.D. Watkins, "Optical detection of electron paramagnetic resonance for intrinsic defects produced in ZnO by 2.5-MeV electron irradiation in situ at 4.2 K," *Phys. Rev*. B 72, 035203 (2005) 035203.

[37] D. Sanyal, T.K. Roy, M. Chakrabarti, S. Dechoudhury, D. Bhowmick, and A. Chakrabarti, "Defect studies in annealed ZnO by positron annihilation spectroscopy," *J. Phys. Condens. Matter* 20 (2008) 45217.

[38] S. Dutta, M. Chakrabarti, S. Chattopadhyay, D. Jana, D. Sanyal, and A. Sarkar, "Defect dynamics in annealed ZnO by positron annihilation spectroscopy," *J. Appl. Phys*. 98 (2005) 53513.

[39] X.J. Liu, C. Song, F. Zeng, X.B. Wang, and F. Pan, Influence of annealing on microstructure and magnetic properties of co-sputtered Co-doped ZnO thin films," J. Phys. D 40 (2007) 1608–1613.

[40] A.K. Mishra, S.K. Chaudhuri, S. Mukherjee, A. Priyam, A. Saha, and D. Das, "Characterization of defects in ZnO nanocrystals: photoluminescence and positron annihilation spectroscopic studies," *J. Appl. Phys*. 102 (2007) 103514.

[41] F. Wang, W.-W. Huang, S.-Y. Li, A-Q. Lian, X.-T. Zhang, and W. Cao, "The magnetic properties of $Fe_xZn_{1-x}O$ synthesized via the solid-state reaction route: Experiment and theory," *J. Magn. Magn. Mater*. 340 (2013) 5–9.

[42] T. Akilan, N. Srinivasan, and R. Saravanan, "Structural and magnetic studies on Fe doped zinc oxide, $Zn_{1-x}Fe_xO$ synthesized by solid state reaction," *J. Mater. Sci.: Mater. Electron.* 26 (2015) 9882–9890.

[43] A. Punnoose, J. Hays, A. Thurber, M.H. Engelhard, R.K. Kukkadapu, C. Wang, V. Shutthanandan, and S. Thevuthasan, "Development of high-temperature ferromagnetism in SnO_2 and paramagnetism in SnO by Fe doping," *Phys. Rev*. B 72 (2005) 054402.

[44] R. Zboril, M. Mashlan, and D. Petridis, "Iron (III) oxides from thermal processes synthesis, structural and magnetic properties, Mössbauer spectroscopy characterization, and applications," *Chem. Mater*. 14 (2002) 969–982.

[45] S.K. Misra, S.I. Andronenko, A. Thurber, A. Punnoose, A. Nalepa, "An X- and Q-band Fe^{3+} EPR study of nanoparticles of magnetic semiconductor $Zn_{1-x}Fe_xO$," *J. Magn. Magn. Mater*. 363 (2014) 82–87.

[46] K. Nomura, C.A. Barrero, J. Sakuma, M. Takeda, "Room-temperature ferromagnetism of sol-gel-synthesized $Sn_{1-x}{}^{57}Fe_xO_{2-\delta}$ powders," *Phys. Rev*. B 75 (2007) 184411.